NANO LETTERS

Letter

pubs.acs.org/NanoLett

# Optoelectromechanical Multimodal Biosensor with Graphene Active Region

Alexander Y. Zhu,[†] Fei Yi,[†] Jason C Reed,[†] Hai Zhu,[†] and Ertugrul Cubukcu*[,†,‡]

[†]Department of Materials Science and Engineering and [‡]Department of Electrical and Systems Engineering, University of Pennsylvania, Philadelphia, Pennsylvania 19104, United States

Supporting Information

**ABSTRACT:** A general, overarching theme in nanotechnology is the integration of multiple disparate fields to realize novel or expanded functionalities. Here, we present a graphene enabled, integrated optoelectromechanical device and demonstrate its utility for biomolecular sensing. We experimentally achieve an ultrawide linear dynamic sensing range of 5 orders of magnitude of protein concentration, an improvement over state-of-the-art single mode nanosensors by approximately 2−3 orders of magnitude, while retaining a subpicomolar lowest detection limit. Moreover, the ability to monitor and characterize adsorption events in the full optoelectromechanical space allows for the extraction of key intrinsic parameters of adsorbates and has the potential to extend the capabilities of nanosensors beyond the traditional binary-valued test for a single type of molecule. This could have significant implications for molecular detection applications at variable concentrations, such as early disease detection in biomedical diagnostics.

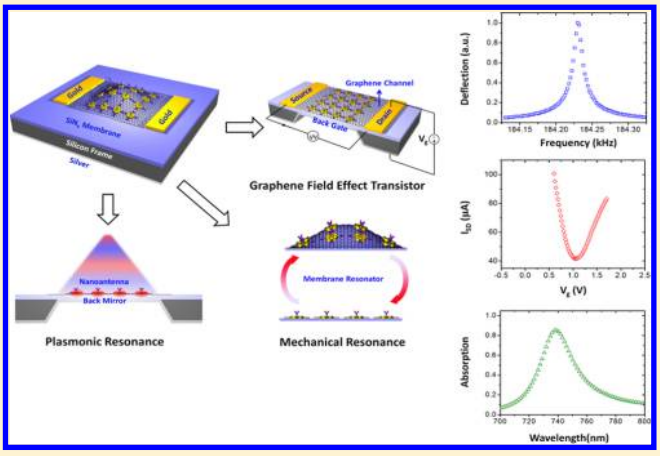


**KEYWORDS:** *Graphene, biosensor, plasmonics, nanomechanics, electrical sensing*

Recent developments in nanotechnology have led to unprecedented advances, both in terms of improving existing device performance and establishing novel functionalities, in a diverse range of disciplines. Within the context of bioanalytics, nanosensors based on plasmonic nanostructures,[1−8] nanomechanical cantilevers,[9−14] carbon nanotubes,[15−18] semiconductor nanowires,[19−22] and graphene[23−29] have been shown to possess exquisite sensitivities down to the single molecular limit,[4,10,12,28] a high spatial resolution for extremely localized detection, and a relatively fast analysis time. This has in turn given rise to the possibility of rapid and potentially low-cost point-of-care diagnostics for medical screening, among other applications.[30]

Existing sensing platforms are predominantly single-mode devices that transduce only one type of signal through specific molecular conjugation.[3,9,21,29] In this case the sensor surface is functionalized with the appropriate binding molecules which preferentially bind to the target analyte, causing a change in the functional property of the device. In addition to serving as a binary valued test for the presence of these molecules, the magnitude of the functional property change can be also used to determine their concentration. However, this single-mode sensing approach has two main limitations: first, it is subject to a necessary trade-off between molecular sensitivity and (linear) dynamic range. The latter is fundamentally constrained by the ratio of perturbative to original sensor response, which must be large in order to possess a high sensitivity, but this in turn lowers the saturation limit. As a result the effective sensor operation range for single mode sensors is typically only 2−3 orders of magnitude of the target protein concentration.[3,9,19,21] Second, the adsorption of biochemical molecules is quintessentially a multiphysics process that simultaneously generates localized perturbations in mass, dielectric permittivity, and electrical conductance, to name a few commonly measured quantities. By definition, single mode devices are only able to capture information about a single property.

Here, we demonstrate a novel nanoscale sensing device with optical, electronic and mechanical functional elements integrated on the same chip. By having each element target a different concentration regime, the sensitivity-dynamic range trade-off of traditional single mode sensors can be significantly mitigated. This works in general for typically reported configurations in each sensing mode, distinguishing it from other techniques that are tailored for a specific type of device, that is, nanocrystal based sensors.[31] Furthermore, the synergistic operation of these sensing modes enables one to monitor and characterize adsorption events in the full optoelectromechanical parameter space. Multiple key parame-

**Received:** June 18, 2014
**Revised:** September 2, 2014

ACS Publications © XXXX American Chemical Society



dx.doi.org/10.1021/nl502279c | *Nano Lett.* XXXX, XXX, XXX−XXX

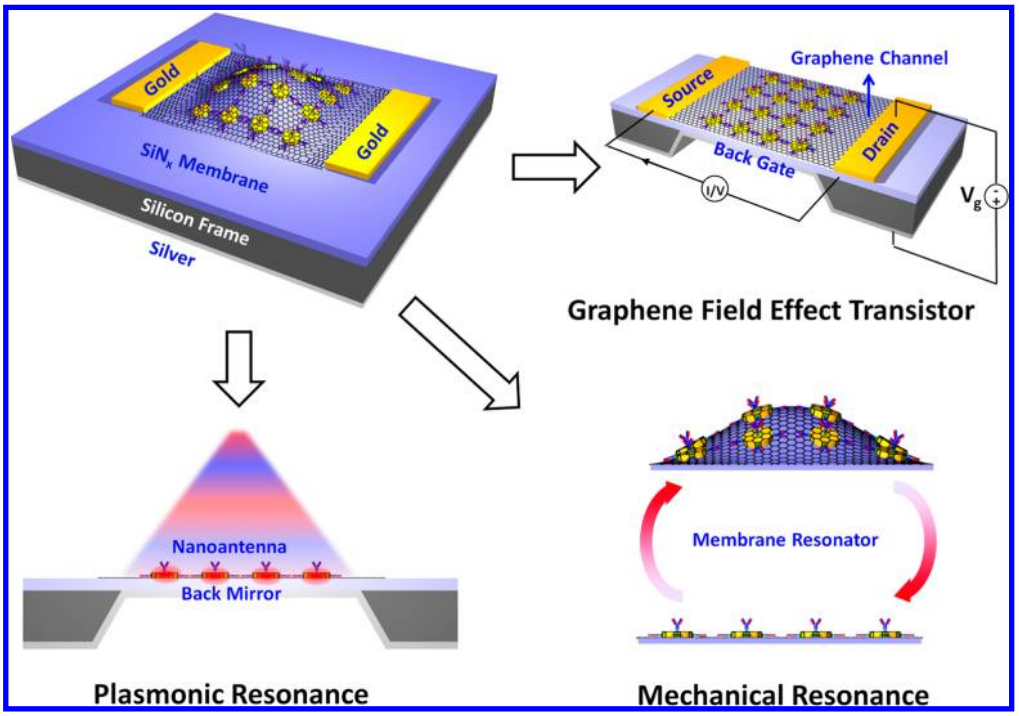


**Figure 1.** Schematic of device structure, starting with angled top view of the sensor chip, comprised of a freestanding silicon nitride membrane suspended over an etched silicon frame. Plasmonic nanodisk antenna, top electrodes, a silver backgate, and graphene are subsequently introduced. Electrical sensing is accomplished by standard operation of the device as a graphene FET. The three subsequent modes of operation are shown: plasmonic resonance sensing via standard optical spectroscopy, detection of doping levels in the graphene FET channel by $I-V$ gating, and mass sensing by probing the resonance position of the fundamental membrane mechanical resonance mode. All three modes of operation can be achieved on the same device platform.

ters intrinsic to the adsorbed molecules, such as mass, surface dissociation constant, binding affinity, and characteristic optical or electrical surface sensitivities can thus be obtained from the individual characterization curves (provided in subsequent sections) on a single device. This greatly expanded functionality could potentially enable the detection and differentiation of multiple protein molecules, through the use of appropriate target-receptor molecules.

The device (Figure 1) consists of a freestanding low stress silicon nitride membrane clamped on all sides to a silicon frame, a configuration capable of supporting high quality ($Q$) factor mechanical resonance modes which are highly sensitive to adsorbed mass.[32] It also serves as a structural support for the subsequent introduction of plasmonically active gold nanodisk antennae and graphene monolayer transferred onto the top surface. The nanoantennae enable surface refractive index sensing via their spectrally resonant electromagnetic near-fields,[3,7,33] while the graphene acts as a traditional field effect transistor (FET) sensing channel[23,25,27,28] and bioactive interface for protein adsorption. A thin (~100 nm) metal coating on the underside of the membrane serves as the gate electrode (with the membrane itself as the gate dielectric).

To obtain a better physical understanding for each of these sensing modalities, we explicitly identify the dependence of each functional property on the amount of adsorbate. For mass sensing, the resonant frequencies of a thin rectangular membrane can in general be written $f_{i,j} = [(i^2 + j^2)/2]^{1/2} f_{1,1}$ where $i,j$ are integer mode indices indicating the number of antinodes for the two in-plane dimensions, and $f_{1,1} = (1/2\pi)(k/\beta_{1,1}m)^{1/2}$ is the fundamental resonance mode.[14,32] $k$ and $\beta$ are constants related to the membrane spring constant and mode modifiers to the mass; the latter arises because not all added mass contributes equally to the resonant frequency of the membrane, depending on the mode profile of the particular chosen resonance. Then straightforwardly any small changes to membrane mass causes perturbations to frequency of the form

$$\Delta f \propto -\frac{\Delta m}{m_\Omega^{3/2}} \propto -Q\frac{\Delta m}{m_\Omega^2} \quad (1)$$

where $m_\Omega$ is the original mass of the membrane oscillator, $\Delta m$ is the added mass, and $Q = [(mk)^{1/2}/D]$ ($D$ being the damping coefficient) is the mechanical quality factor of the membrane, which describes the ratio between stored and dissipated power in the system. We therefore seek a resonator with a low initial starting mass and low loss (high $Q$ factor). Experimental characterization of our pristine device before analyte addition demonstrates a fundamental mode resonance with $Q \sim 10^4$ (Figure 2a), a value broadly comparable to specialized high $Q$ on-chip micromechanical resonators.[34]

Similarly, graphene is used as the active material for electrical-based sensing mode in our device due to its high carrier mobility and surface-to-volume ratio (being a two-dimensional material), low electrical noise (in the case of defect-free crystals),[35] as well as low initial carrier concentration;[28] these are essentially the same benefits that motivated research into carbon nanotube and semiconductor nanowire sensors.[18−22] In addition, its relative ease of large-scale preparation via chemical vapor deposition (CVD) and ability to be transferred onto most substrates affords it unique advantages over the aforementioned nanowires. Because of the unique band-structure of graphene, the Fermi energy is directly related to the square root of its carrier concentration $n$ via $E_F = \hbar|v_F|(\pi n)^{1/2}$.[36] The latter quantity can be significantly changed


dx.doi.org/10.1021/nl502279c | Nano Lett. XXXX, XXX, XXX−XXX

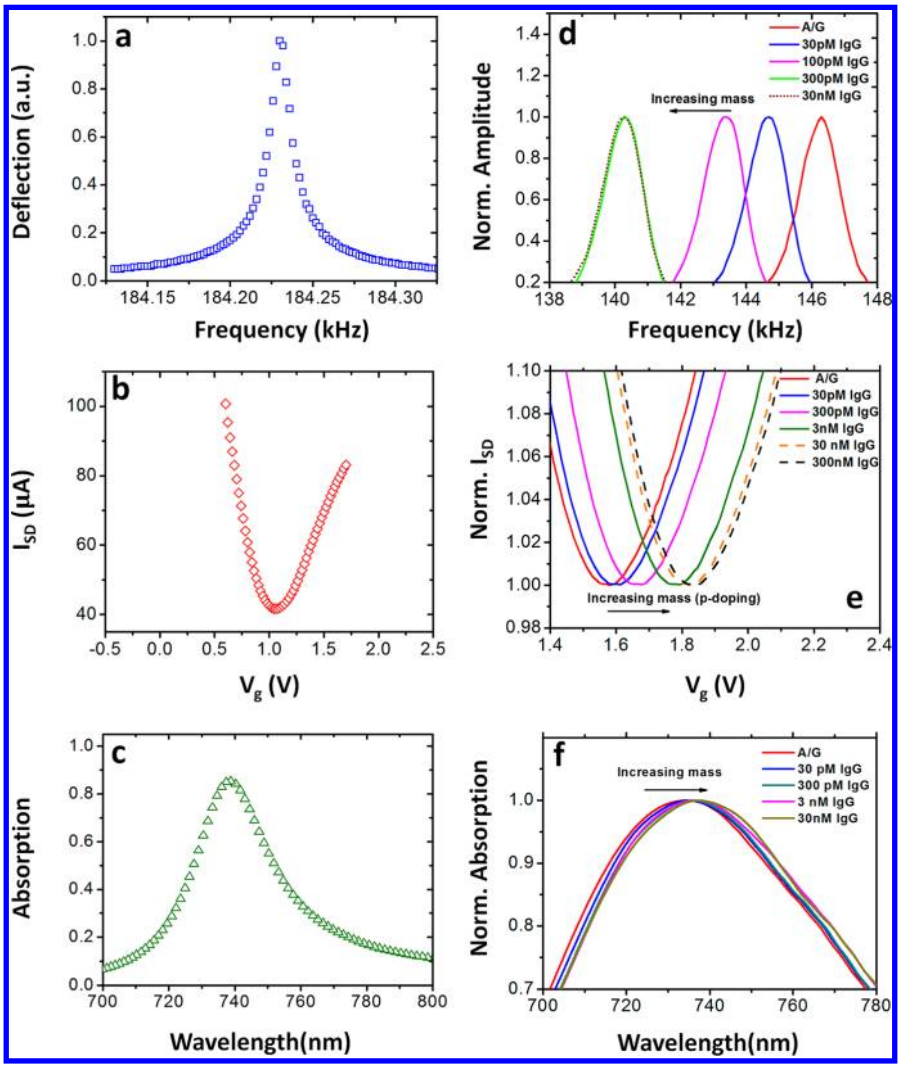


**Figure 2.** Pristine and functionalized device characterizations. (a–c) Mechanical, electrical, and optical responses of a pristine device sample, respectively. (d–f) Sensor responses in response to protein binding of the fundamental mechanical resonance mode, graphene FET source-drain current–voltage characterization, and localized surface plasmon resonance of Au nanodisks, respectively. Data for each particular concentration are obtained from the same protein addition on the same sample, clearly illustrating signal transduction using all three independent sensing modes.

by surface adsorbates, via either direct-charge transfer or electrostatic double layer gating effects, which forms the basis for various graphene FET type sensors described in the literature.[23,25,27,28] Here we adopt a slightly different approach to track the position of the Fermi level itself with varying levels of adsorbate (where $\Delta n$ is the differential change in carrier concentration)

$$\Delta E_F \propto |v_F| \frac{\Delta n}{\sqrt{n}} \tag{2}$$

by performing consecutive $I-V$ sweeps of the device at different adsorbate concentrations, and quantifying the change in the minimum conductivity as a function of applied gate voltage (which arises when the number of injected carriers exactly balance the intrinsic and adsorbate-induced doping levels of the graphene (i.e., where the Fermi energy rests at the Dirac point, also termed the charge neutrality point or CNP). Characterization results of pristine devices (Figure 2b, Supporting Information Figure S1) indicate high quality graphene crystals with a CNP of 1 V, corresponding to an excess electron concentration of $\sim 10^{11}/\mathrm{cm}^2$.

Finally, subwavelength metallic nanostructures are known to support localized surface plasmon resonances due to the collective oscillations of the electron plasma coupled to light.[3] For discrete nanosized particles, the electron oscillation is confined to the particles (i.e., localized). The strong confinement of these electromagnetic modes near the nanoantenna results in significantly enhanced optical near field intensities. These optical resonances depend strongly on the refractive index of the surrounding dielectric medium. Together, these properties form the basis for plasmonic sensing by detecting the perturbations to the surface refractive index or dielectric permittivity due to the adsorbates, which can be measured by determining the optical resonant frequencies of scattering or extinction. Intuitively, in the quasi-static limit (where particle size is much less than incident wavelength) and assuming a simple Drude model for the noble metal, the resonant frequency change can be written

$$\Delta\lambda_{max} \propto \lambda_p \frac{2n_d}{\sqrt{2n_d^2 + 1}} \Delta n_d \tag{3}$$


dx.doi.org/10.1021/nl502279c | Nano Lett. XXXX, XXX, XXX–XXX

where $\lambda_p$ is the wavelength corresponding to the (bulk) plasma frequency of the metal nanostructures and $n_d$ is the refractive index of the surrounding dielectric medium. Note that here the presence of the $\Delta n_d$ term is a simplification: it represents the spatially averaged change in permittivity due to the adsorbates, but strictly this is only true for the sensor surface as the bulk medium remains the same. Rigorously $\Delta n_d$ therefore contains terms that quantify the degree of electric field overlap with the adsorbates at the surface; sensitivity thus depends very much on the geometry, size, and chosen material for the plasmonic structures. In addition, a commonly used figure of merit for plasmonic sensors divides the peak wavelength sensitivity ($d\lambda/dn$) by the full width at half-maximum (fwhm) of the plasmonic resonance peak (or equivalently multiplying by optical $Q$ factor), because the latter determines the minimum detectable change in peak wavelength shift. In our device we were able to observe a surface plasmon resonance enhanced near-unity absorption due to the coupled nanoantennae-optical cavity configuration with a relatively high optical $Q$ of ~25 (Figure 2c).[37]

From the previous analysis, it can be seen that this device architecture also exploits multiple synergies: besides the silicon nitride membrane that doubles as a high $Q$ mechanical resonator and relatively high-$k$ gate dielectric, the silver gate electrode also functions as a back reflector to the plasmonic nanoantennae, whose resonance lie at approximately 740 nm. This suppression of optical transmission results in a cavity enhanced resonance peak, increasing optical $Q$, and sensitivity. This can be understood intuitively as the optical cavity configuration suppresses the outgoing reflected waves via destructive interference and greatly increases the number of round trips made by incident light, resulting in larger absorption, longer confinement time (as well as photon lifetime in the structure) and field intensity at the surface (for an approximately quarter-wavelength cavity the field antinode is at the surface, as is the case here). Lastly, in addition to functioning as a FET sensor, graphene also significantly increases the surface (bio)molecular adsorption limit in general due to a large specific surface area, high polarizability relative to dielectric substrates, and $\pi-\pi$ interactions with hydrocarbon chains in biomolecules.[38,39] Moreover, due to its atomically thin nature it does so without significantly perturbing the optical and mechanical detection modes, thus greatly enhancing their net sensitivities and enabling multicomponent integration. Further details on graphene functionality are presented in the Supporting Information (Figures S1 and S2).

We first characterized device performance for traditional specific target-receptor type conjugation to ensure that the integration process does not significantly compromise the individual functionality of each sensing channel. Label-free end-point protein detection trials were carried out using murine immunoglobulin G (IgG) with recombinant protein A/G as the specific binding intermediary. In these experiments, the sensor surface is first saturated with the binding protein in order to measure the sensor response (of each mode) that arises from the specific binding of the IgG antibody at various concentrations. The sensor responses are separately monitored across the different modes after an incubation time of 1.5 h for each concentration level. For the mechanical mode, the fundamental resonance frequency linearly shifts to lower values as the protein concentration is increased in the ~10 pM range, which is in agreement with eq 1 (Figure 3a). A linear fit to the mechanical frequency response in this range leads to a sensitivity of 23.7 Hz/pM with a minimum noise-limited detectable concentration of approximately 0.5 pM. The integrated nanoelectronic sensing response of the graphene FET is characterized by measuring the current voltage ($I-V$)

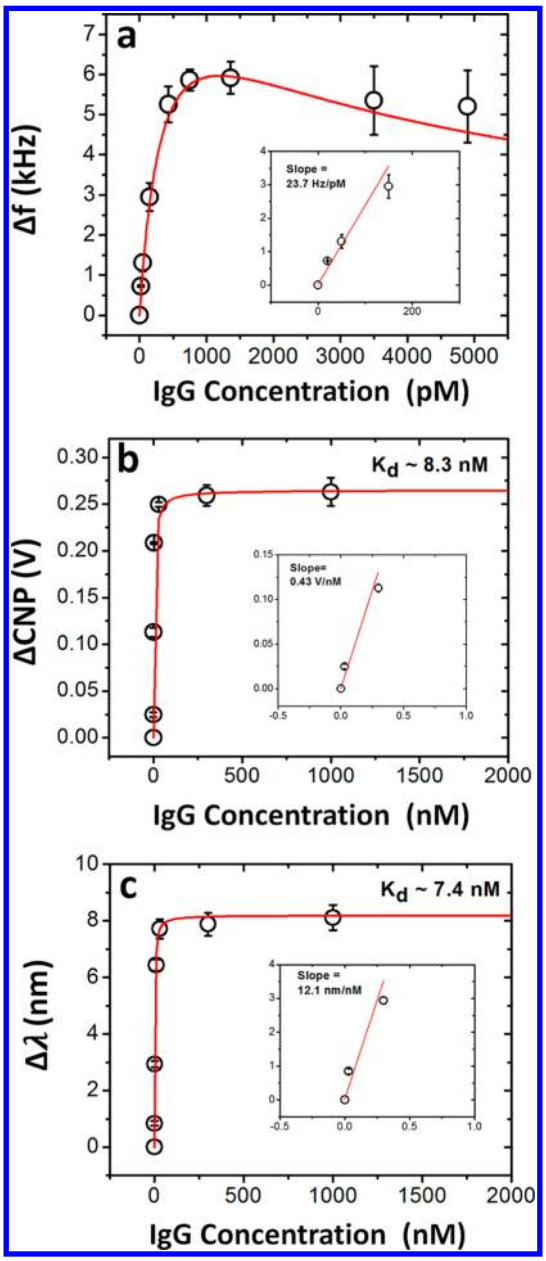


**Figure 3.** Langmuir adsorption isotherms for A/G–IgG device response. Characterization curves after functionalizing with protein A/G, as a function of added IgG. Panels (b,c) were averaged over six samples and fitted with eq 1, while panel (a) was averaged over three samples and fitted with eq 2. Two devices were common to all three sets of measurements. Error bars indicate one standard deviation. Inset: Linear fit to the first few data points of each sensing mode, before significant saturation (deviation of slope of more than 10%) of the response occurs. The sensitivity is defined as the slope of this linear fit, which captures the initial response of the nanosensor. The individual linear dynamic range (defined from minimum detectable concentration to the concentration closest to the turning point of the respective response curves) is approximately 0.5 pM to 1 nM for the mechanical sensing mode and approximately 30 pM to 30 nM for both electrical and optical modes, yielding a combined linear dynamic range from subpicomolar to tens of nanomolar.


dx.doi.org/10.1021/nl502279c | Nano Lett. XXXX, XXX, XXX–XXX

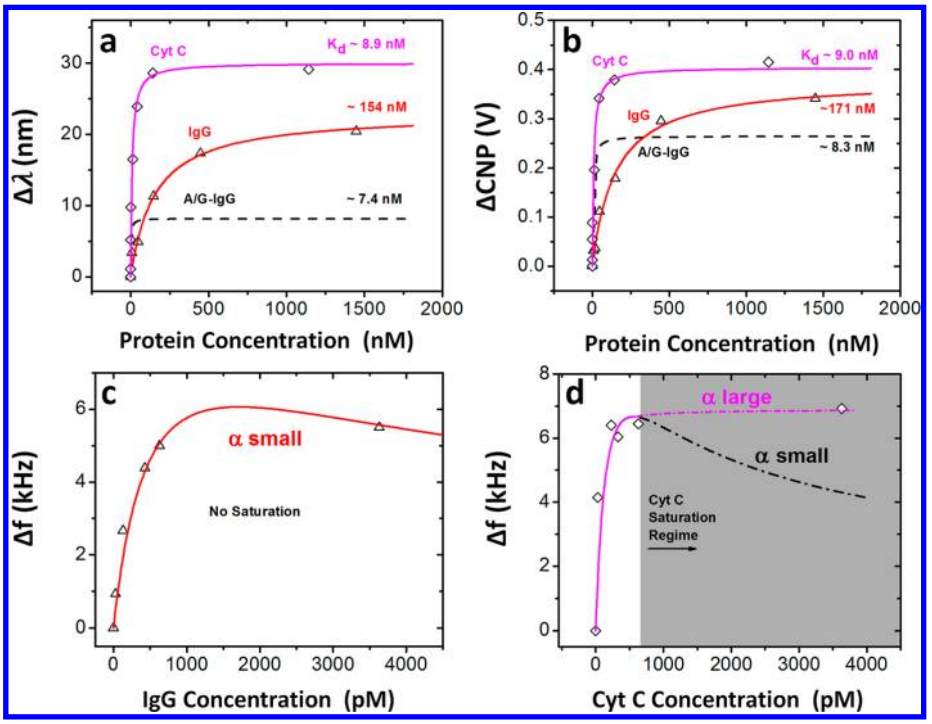


**Figure 4.** Unconjugated IgG and Cyt C characterizations. (a,b) Optical and electrical characterization curves on separate devices without A/G functionalization. Previous A/G−IgG results are shown in black dotted lines. (c,d) Mass characterizations of unconjugated IgG and Cyt C. Saturation of graphene surface during Cyt C addition is shown by shaded region, resulting in a large $\alpha$ (as defined in eq 5) and hence apparent "saturation" of the mass response.

characteristics of the device for various concentrations of IgG. As discussed in the introduction, the $I-V$ curve exhibits a zero-slope feature corresponding to the charge neutrality point of the graphene channel (Figure 3b). Monitoring the shift in the Fermi level in the electrical measurements allows us to quantify the amount of adsorbed protein and the corresponding concentration for the given incubation time. Although the electrical measurements are performed on the same device following mechanical characterization, there was no observable change in the electrical response for concentrations less than approximately 30 pM, which is limited by the electrical noise. For detectable concentrations, the electrical response is also linear as predicted by eq 2, yielding a sensitivity of 0.43 V/nM. Finally, optical measurements are performed by illuminating the active device area at normal incidence, exciting the spectrally resonant modes of the nanoantennae. Adsorption of biomolecules causes a change in the local refractive index, causing a shift in the position of the plasmon resonance peak that can in turn be related to the added concentration, as in eq 3. For optical measurements, the initial sensitivity of the device is found to be 12.1 nm/nM, which translates to an instrument-limited minimum detection limit of approximately 30 pM as well (Figure 3c).

In general these values are comparable with their state-of-the-art, single mode counterparts of similar structure and design.[7,9,23,40] More importantly, the overall linear dynamic range (defined from the minimum detectable concentration of the overall device, to the concentration closest to the turning point of the response curves as shown in Figure 3) is also 5 orders of magnitude. This is 2−3 orders of magnitude higher than what most traditional single mode devices,[3,7,9,21,23] or any individual sensing mode on our device can achieve, by virtue of the distinct (but overlapping) target concentration regimes of the individual sensing modalities. For example, as mentioned in the preceding section, for our proof-of-concept device the individual linear dynamic range is approximately 0.5 pM to 1 nM for the mechanical sensing mode and approximately 30 pM to 30 nM for both electrical and optical modes, yielding a combined range from subpicomolar to tens of nanomolar.

In order to be able to quantify the concentration of analyte present by looking at the sensor response, an analytical relation between the two needs to be established. Figure 3 reveals qualitatively different sensing responses: the optical and electrical responses (Figure 3b, c) are seen to plateau and effectively saturate at ~10 nM concentrations, while the mass response (Figure 3a) peaks approximately an order of magnitude earlier and subsequently decreases. This behavior arises as the responses are due to fundamentally different mechanisms: optical and electrical responses are due to local permittivity perturbations and graphene doping, respectively, which scale with fractional protein surface coverage and is well-described by the Langmuir adsorption isotherm[41]

$$\Delta = \frac{\Delta_{max}[C]}{K_d + [C]} \tag{4}$$

where $\Delta$ is the instantaneous response, $\Delta_{max}$ is the saturation response, $[C]$ is the protein concentration, and $K_d$ is the Langmuir equilibrium constant of dissociation. Notably, $K_d = (k_{off}/k_{on})$ characterizes the strength of the binding event and is an indication of the surface affinity between the binding surface (here, the graphene) and adsorbate and is equivalent to the ratio of the (dynamic) rates of desorption ($k_{off}$) and adsorption ($k_{on}$). It ought to be emphasized that although the measurements are serial, the long incubation times and subsequent quick postincubation washes of the spotting process (see Methods) ensures that local equilibration of the protein


dx.doi.org/10.1021/nl502279c | Nano Lett. XXXX, XXX, XXX−XXX

molecules with the sensor surface is achieved during incubation and "frozen-in" after the wash; the measurements can thus be understood as taking a snapshot of an otherwise real-time sensing trial, and the data are expected to follow the Langmuir isotherm. In addition, we observe that the fitted values of $K_d$ for optical and electrical measurements agree well with each other (Figure 2e, f). These values are also in agreement with other reported values in the literature for conjugated molecular binding.[19,42]

In contrast, therefore, the mass response cannot be saturated at subnanomolar concentrations. The peak and subsequent decrease must thus arise due to the physics of the mechanical resonance itself. Rewriting eq 1 in terms of the concentration of adsorbates, we obtain

$$\Delta f \approx \frac{\kappa}{4\pi}\frac{[\mathrm{C}]}{\left[\frac{\beta_1 K_d m_\Omega}{\beta_2 A \Gamma_{max} M_r} + [\mathrm{C}]\right]^{3/2}} = \frac{\kappa}{4\pi}\frac{[\mathrm{C}]}{\left[\frac{\beta_1 m_\Omega}{\beta_2 \alpha M_r} + [\mathrm{C}]\right]^{3/2}} \quad (5)$$

where $m_\Omega$ is the original bulk mass of the membrane resonator, $K_d$ is the Langmuir equilibrium dissociation constant as defined in eq 4, $\Gamma_{max}$ is the number of binding sites (in moles per unit area), $A$ the effective surface area of the sensor, $\beta_1$ and $\beta_2$ are the constant modifiers to the membrane and added masses respectively, based on the mode profile of the measured resonance (here always the fundamental mechanical resonance), $M_r$ is the molar mass of adsorbents, and $\kappa$ is a phenomenological constant, taking into account initial stresses or deflections of the membrane. This equation can be straightforwardly derived from the standard equation of a resonator,[10,14] without neglecting any higher order terms. Also $\beta_1 = \beta_2$ under the assumption that the adsorbed masses possess a spatially homogeneous distribution, that is, there are no local stress centers. In addition, we can define a quantity $\alpha = (A\Gamma_{max}/K_d)$ which is determined exclusively by the nature of the sensor and type of adsorbate, which characterizes the effective "strength" of an interaction. By inspecting the final form of eq 5, we see that it accurately predicts the appearance of a local maximum in the mass response if $\alpha$ is large, or an essentially constant line if $\alpha$ is small, resulting in a highly similar visual appearance to the Langmuir adsorption isotherm (Supporting Information Figure S4).

As an additional proof of concept to demonstrate the potential of our device for protein differentiation purposes, we characterized two different proteins, murine IgG and oxidized cytochrome-c (Cyt C) from equine heart, in the optoelectromechanical 3D parameter space (Figure 4a–d). No intermediary binding protein was used, that is, no specific molecular conjugation in order to extract intrinsic properties of the proteins when adsorbed directly onto graphene. Consequently $K_d$ for IgG increased to 154 nM from 7.4 nM (Figure 4a) and 171 nM from 8.3 nM (Figure 4b) for optical and electrical measurements respectively, indicating a much weaker surface binding affinity between the protein and graphene. Cyt C on the other hand is found to possess a fairly low $K_d$ of approximately 9 nM, only marginally weaker than the A/G–IgG binding strength.

Results from the mass sensing component for IgG and Cyt C (Figure 4c,d) corroborate the optical and electrical results. Using eq 2, the relevant fitting parameter for mass responses is the quantity $(m_\Omega/\alpha M_r)$ that is found to be $\sim 1.25 \times 10^{-5}$ and $9.05 \times 10^{-5}$ mol dm$^{-3}$ for IgG and Cyt C, respectively. This implies a difference in $\alpha$ (and hence $K_d$, assuming that the number of available sites do not significantly vary for the same device) of ~25 times, taking into account their respective molar masses of 160 and 12 kg. This is consistent with the ratio of $K_d$ of the two proteins (approximately 20 times) obtained from the unconjugated graphene binding experiments in the optical and electrical modes as described previously; differences likely arise because $K_d$ by definition assumes ideal equilibration between the protein and the surface, whereas practically the equilibration process is subject to environmental factors such as pH fluctuations and variations in surface hydrophobicity.

We first comment that the measured affinities of A/G–murine IgG binding as presented in the main text, characterized by the Langmuir dissociation constant, are in excellent agreement with protein-receptor binding values in the existing literature.[19,42] As mentioned in the main text, both the binding affinities and the saturation responses of IgG and Cyt C can be understood by considering their chemical structure and the subsequent interaction with graphene.

The oxidized Cyt C molecule is essentially an $Fe^{3+}$ ion complex surrounded by a highly conjugated porphyrin ring.[43] Because of the innate conjugation and the small size of the molecule, the electron orbitals in Cyt C are able to readily and significantly overlap with the extended $\pi$-orbitals of graphene. The $Fe^{3+}$ ion further contributes to this as its valence electrons occupy the highly penetrating 3d subshells. This results in a comparatively strong attraction to the graphene surface, as borne out by extensive theoretical studies using ab initio and density functional theory (DFT) calculations of similar phenomena.[44−48] In contrast, IgG being a massive chain molecule exhibits no such preferential bonding and orbital overlap; its Y-shaped geometry and size (~10 times greater than Cyt C[49]) are further likely to cause steric hindrance to subsequent molecules that attempt to bind to neighboring sites. Thus, the only factors that lower adsorption energy are inductive effects due to the large and therefore relatively polarizable electron cloud. As a result we observe the clear discrepancy in binding strengths to graphene, as shown in Figure 4a–d.

The difference in binding strengths give rise to the qualitatively different behavior under mass testing, as discussed in the previous sections. It is interesting to consider what gives rise to the difference in saturation response for the optical and electrical sensing modes (Figure 4a, b). Optically, the resonance peak shift is determined by both the magnitude of the local index change and the volume degree of interaction with the plasmonically enhanced near field. Cyt C has a larger refractive index of ~1.6 but a much smaller size compared to IgG (refractive index ~1.3).[49,50] While it is not immediately clear a priori which molecule would have the larger shift as quantitative information regarding field mode volume of our fabricated structures is unknown, we can certainly rationalize the (optical) experimental results (Figure 4a); the mode confinement of the gold nanodisk antenna was such that the greater interaction length with IgG dominates. One can expect that for more confined fields, such as those occurring in higher order multipole resonances, the situation may be reversed. Similarly, we can attribute the higher saturation electrical response to the larger number of Cyt C molecules adsorbed; though the relatively significant orbital overlap with graphene enables direct charge transfer from graphene to the oxidized Cyt C molecule,[51] the capacitative gating effect due to IgG is apparently greater per unit mass adsorbed.


dx.doi.org/10.1021/nl502279c | Nano Lett. XXXX, XXX, XXX–XXX

By being able to obtain consistent data in all three sensing modes from individual protein additions, we have extracted unique parameters such as binding and dissociation constants, optical and electrical surface sensitivities, as well as saturation responses for IgG and Cyt C molecules. Though in this case these molecules were intentionally chosen to be distinct in terms of mass, molecular size, refractive index, and electronic charge, it follows that one would be able to categorically differentiate between (unconjugated) molecules which are similar in one or more aspects (but not all three). This could also potentially form the basis for a unique protein identification scheme, through the establishment of a library of such data.

We conducted an additional experiment emulating the case where a single mode mass sensor would fail in a complex biomolecular mixture containing two distinct proteins that generated the same mass perturbations (to within error). We performed pseudorandom, sequential spotting of IgG and Cyt C onto the same samples, with concentrations chosen such that the total adsorbed mass for each type of molecule was the same, that is, they resulted in similar mechanical shifts (with an averaged difference of ∼14%) of the membrane resonator (Supporting Information Figure S5). Clearly, the addition of approximately the same mass of Cyt C produced no significant sensor response (below the noise level) in the electrical and optical modes compared to IgG; the signal contrast is an order of magnitude different for the two types of molecules. These results are also consistent with the characterization data shown in Figure 3, where the larger saturation responses of Cyt C are primarily due to its significantly larger binding constant.

In conclusion, we have demonstrated a graphene-based multimodal biosensing device, capable of transducing protein binding events into optical, electrical, and mechanical signals. The device is found to possess detection limits comparable to its single mode counterparts for specific conjugation and exhibits a large linear dynamic sensing range. Preliminary results with unconjugated sensing suggest that the device could also be eventually used to differentiate and, ideally, identify multiple distinct biomolecules, as long as the design is modified to have a sufficient sensitivity and temporal resolution and support simultaneous measurements.

**Methods.** *Sensor Fabrication.* Low-stress LPCVD deposited silicon nitride membranes (100 nm thickness) on silicon with a pre-etched window of 500 $\mu$m × 500 $\mu$m were purchased (Norcada, Inc.). These were subsequently cleaned by oxygen plasma. Periodic disk nanoantenna (diameter, 130 nm; period, 210 nm) and surface source and drain electrodes were introduced by spin-coating a PMMA 495/950 resist bilayer, followed by electron beam lithography (Elionix ELS-7500EX). Ti/Au (3/30 nm) were subsequently deposited using an electron beam evaporator (Kurt Lesker PVD-75). Liftoff was performed at 75 °C in Microposit Remover PG bath, followed by IPA and DI water rinse. Fifty nanometers of Ag was deposited on the underside of the device to form the gate electrode. Note that Ag was used instead of a more inert metal such as gold due to the latter's interband transitions in the 630 nm wavelength regime. Samples were stored under vacuum conditions at all times except during optical and electrical testing, and protein additions. To allay concerns about possible sulfidation effects, an additional 20 nm of Au was deposited for the final batch of samples (used for the IgG/Cyt C distinguishing tests) as a passivation layer; identical results to within experimental error were obtained (Supporting Information Figure S6).

CVD graphene on copper foils was purchased from Graphene Supermarket, and mechanically trimmed to desired sizes of greater than the eventual FET channel width. They were then spin-coated with PMMA 495 and baked to maintain structural integrity after etching. Etching was done using Transene APS 100 solution (active ingredient: ammonium peroxodisulfate) for relatively clean etching of copper. The graphene/PMMA pieces were mechanically transferred to the FET channel region of the devices; these are subsequently baked at 150 °C, repeatedly rinsed in acetone/IPA and held for a prolonged period at 200 °C for resist stripping and residue removal. The measured low doping levels of $\sim 10^{11}$ cm$^{-2}$ and Raman spectrum (Supporting Information Figure S1d) suggest relatively clean and defect free graphene was obtained as-transferred.

*Protein Preparation and Addition.* Murine (mouse) antibody IgG and its binding conjugate A/G were purchased (Pierce) and sequentially diluted to desired concentrations in standard phosphate-buffered saline solution (PBS buffer). Concentrations used were 0.01 and 0.1 M, respectively, to keep each protein in the same chemical environment as their respective native (stock) conditions. Oxidized Cyt C from equine heart (Sigma-Aldrich) was prepared as-received in a similar manner in 0.01 M PBS. Protein additions were accomplished by spotting; 2 $\mu$L of solution is withdrawn and spotted on the active area of the device by micropipette. and the drop is then incubated in protected, environmental hood conditions. Typical incubation times are 1.5 h. Samples are then washed in a fresh PBS solution followed by DI water in order to remove excess protein and PBS.

*Measurement and Characterization.* Optical measurements were performed using a home-built microscopy setup. A fiber coupled broadband white light source (OceanOptics LS-1) was collimated and focused onto the active area of the sample with a 50× objective (Mitutoyo, 0.42 NA). The reflected light is passed back through the objective and a beam splitter and was imaged by a tube lens (Mitutoyo) and focused by a 10× objective (Olympus, 0.25 NA) into a fiber-coupled CCD spectrometer (ThorLabs CCS). All optical spectra taken were referenced against the unpatterned region of the membrane devices; actual power values were obtained by normalizing against source power reflected from a broadband dichroic mirror (ThorLabs). Measurements were identically sampled with a 10 ms exposure time and 10× spectral averaging and identically treated with a 50× boxcar smoothing algorithm.

For electrical measurements, samples were reversibly mounted onto a copper-plated chip for easier access to the silver gate electrode. Contacts were made at previously electron-beam deposited source, drain, and gate electrodes using standard micromanipulator controlled gold probe tips. Voltage sweeps were performed by two series connected source-meters (Keithley 2400) at constant source−drain voltage of 100 mV, a step size of 10 mV and a time interval of 5 s/step to allow for hysteresis effects. Data collection was done using a standard LabView software package. Contact and electrode resistances were determined separately through the symmetry of the electrode design and accounted for in final data processing.

Mass measurements were taken by mounting the samples using adhesive PDMS gel strips to a piezo-actuated stage in an evacuated chamber. A standard fiber-optic laser interferometry


dx.doi.org/10.1021/nl502279c | *Nano Lett.* XXXX, XXX, XXX−XXX

setup, based on the Fabry–Perot cavity formed between the facet of a cleaved fiber and the reflective backplate of the sample, was used to optically determine membrane deflections. A low noise 1550 nm laser was coupled into the fiber through a circulator; the reflected light was routed to a small area PIN diode and the resultant electrical signal sent through a lock-in amplifier (Stanford Research Systems) and RF spectrum analyzer (HP 8565).

## ■ ASSOCIATED CONTENT

### Ⓢ Supporting Information

Graphene characterization; noise and detection limits; mass response fitting function; binding affinities and saturation responses of Cyt C and IgG; and protein differentiation tests. This material is available free of charge via the Internet at http://pubs.acs.org.

## ■ AUTHOR INFORMATION


### Corresponding Author

*E-mail: cubukcu@seas.upenn.edu.


### Author Contributions

A.Y.Z. and F. Y. contributed equally.

E.C. conceived the idea, designed the experiment, and took part in analyzing the data. A.Y.Z. helped with experimental design, fabricated the devices, carried out part of the measurements and coanalyzed the data. F.Y. helped in fabrication, carried out the remaining measurements and coanalyzed the data. J.C.R. and H.Z. contributed to device fabrication and characterization procedures. All authors participated in discussions of results and writing of the manuscript.

### Notes

The authors declare no competing financial interest.

## ■ ACKNOWLEDGMENTS

This work was supported partially by the NSF (under IIP-1312202 and ECCS-1408139). Part of this work was carried out in the Penn Wolf and Quattrone nanofabrication facilities, the Nano/Bio Interface Center (NBIC) that receives partial support from the NSF, and the Penn Regional Nanotechnology Facility (PRNF), a member of the NSF-funded Materials Research Facilities Network. The authors thank E. Shim for artwork. A.Y.Z also thanks S. Szewczyk for technical assistance and support.

## ■ REFERENCES


(1) Adato, R.; Altug, H. *Nat. Commun.* **2013**, *4*, 2154.

(2) Adato, R.; Yanik, A. A.; Amsden, J. J.; Kaplan, D. L.; Omenetto, F. G.; Hong, M. K.; Erramilli, S.; Altug, H. *Proc. Natl. Acad. Sci. U.S.A.* **2009**, *106*, 19227–19232.

(3) Anker, J. N.; Hall, W. P.; Lyandres, O.; Shah, N. C.; Zhao, J.; Van Duyne, R. P. *Nat. Mater.* **2008**, *7*, 442–453.

(4) Chen, S.; Svedendahl, M.; Van Duyne, R. P.; Kall, M. *Nano Lett.* **2011**, *11*, 1826–1830.

(5) Kabashin, A. V.; Evans, P.; Pastovsky, S.; Hendren, W.; Wurtz, G. A.; Atkinson, R.; Pollard, R.; Podolskiy, V. A.; Zayats, A. V. *Nat. Mater.* **2009**, *8*, 867–871.

(6) Liu, N.; Mesch, M.; Weiss, T.; Hentschel, M.; Giessen, H. *Nano Lett.* **2010**, *10*, 2342–2348.

(7) Zhao, J.; Zhang, X. Y.; Yonzon, C. R.; Haes, A. J.; Van Duyne, R. P. *Nanomedicine* **2006**, *1*, 219–228.

(8) Salihoglu, O.; Balci, S.; Kocabas, C. *Appl. Phys. Lett.* **2012**, *100*, 213110.

(9) Arlett, J. L.; Myers, E. B.; Roukes, M. L. *Nat. Nanotechnol.* **2011**, *6*, 203–215.

(10) Burg, T. P.; Godin, M.; Knudsen, S. M.; Shen, W.; Carlson, G.; Foster, J. S.; Babcock, K.; Manalis, S. *Nature* **2007**, *446*, 1066–1069.

(11) Fritz, J.; Baller, M. K.; Lang, H. P.; Rothuizen, H.; Vettiger, P.; Meyer, E.; Guntherodt, H.-J.; Gerber, Ch.; Gimzewski, J. K. *Science* **2000**, *288*, 316–318.

(12) Hanay, M. S.; Kelber, S.; Naik, A. K.; Chi, D.; Hentz, S.; Bullard, E. C.; Colinet, E.; Duraffourg, L.; Roukes, M. L. *Nat. Nanotechnol.* **2012**, *7*, 602–608.

(13) Weinstein, D.; Bhave, S. A. The Resonant Body Transistor. *Nano Lett.* **2010**, *10*, 1234–1237.

(14) Lu, Y. R.; Peng, S. M.; Luo, D.; Lal, A. *Nat. Commun.* **2011**, *2*, 1587.

(15) Bethune, D. S.; Kiang, C. H.; De Vries, M. S.; Gorman, G.; Savoy, R.; Vazquez, J.; Beyers, R. *Nature* **1993**, *363*, 605–607.

(16) Collins, P. G.; Bradley, K.; Ishigami, M.; Zettl, A. *Science* **2000**, *287*, 1801–1804.

(17) Iijima, S.; Ichihashi, T. *Nature* **1993**, *363*, 603–605.

(18) Kong, J.; Franklin, N. R.; Zhou, C.; Chapline, M. G.; Peng, S.; Cho, K.; Dai, H. *Science* **2000**, *287*, 622–625.

(19) Cui, Y.; Lieber, C. M. *Science* **2001**, *291*, 851–853.

(20) Cui, Y.; Wei, Q.; Park, H.; Lieber, C. M. *Science* **2001**, *293*, 1289–1292.

(21) Patolsky, F.; Zheng, G. F.; Lieber, C. M. *Anal. Chem.* **2006**, *78*, 4260–4269.

(22) Stern, E.; Vacic, A.; Rajan, N. K.; Criscione, J. M.; Park, J.; Ilic, B. R.; Mooney, D. J.; Reed, M. A.; Fahmy, T. M. *Nat. Nanotechnol.* **2010**, *5*, 138–142.

(23) Dong, X. C.; Shi, Y. M.; Huang, W.; Chen, P.; Li, L. J. *Adv. Mater.* **2010**, *22*, 1649–1653.

(24) Geim, A. K.; Novoselov, K. S. *Nat. Mater.* **2007**, *6*, 183–191.

(25) Mao, S.; Yu, K. H.; Chang, J. B.; Steeber, D. A.; Ocola, L. E.; Chen, J. H. *Sci. Rep.* **2013**, *3*, 1696.

(26) Novoselov, K. S.; Geim, A. K.; Morozov, S. V.; Jiang, D.; Zhang, Y.; Dubonos, S. V.; Grigorieva, I. V.; Firsov, A. A. *Science* **2004**, *306*, 666–669.

(27) Ohno, Y.; Maehashi, K.; Matsumoto, K. *J. Am. Chem. Soc.* **2010**, *132*, 18012–18013.

(28) Schedin, F.; Geim, A. K.; Morozov, S. V.; Hill, E. W.; Blake, P.; Katsnelson, M. I.; Novoselov, K. S. *Nat. Mater.* **2007**, *6*, 652–655.

(29) Shao, Y. Y.; Wang, J.; Wu, H.; Liu, J.; Aksay, I. A.; Lin, Y. H. *Electroanalysis* **2010**, *22*, 1027–1036.

(30) Jain, K. K. *Clin. Chim. Acta* **2005**, *358*, 37–54.

(31) Soleymani, L.; Fang, Z.; Sargent, E. H.; Kelly, S. O. *Nat. Nanotechnol.* **2009**, *4*, 844–848.

(32) Yu, P. L.; Purdy, T. P.; Regal, C. A. *Phys. Rev. Lett.* **2012**, *108*, 083603.

(33) Barnes, W. L.; Dereux, A.; Ebbesen, T. W. *Nature* **2003**, *424*, 824–830.

(34) Lombardi, M. A. In *Mechatronic Systems, Sensors, and Actuators*, 2nd ed.; CRC Press: Boca Raton, FL, 2008.

(35) Balandin, A. A. *Nat. Nanotechnol.* **2013**, *8*, 549–555.

(36) Das, A.; Pisana, S.; Chakraborty, B.; Piscanec, S.; Saha, S. K.; Waghmere, U. V.; Novoselov, K. S.; Krishnamurthy, H. R.; Geim, A. K.; Ferrari, A. C.; Sood, A. K. *Nat. Nanotechnol.* **2008**, *3*, 210–215.

(37) Wu, C.; Neuner, B.; Shvets, G.; John, J.; Milder, A.; Zollars, B.; Savoy, S. *Phys. Rev. B* **2011**, *84*, 075102.

(38) Georgakilas, V.; Otyepka, M.; Bourlinos, A. B.; Chandra, V.; Kim, N.; Kemp, K. C.; Hobza, P.; Zboril, R.; Kim, K. S. *Chem. Rev.* **2012**, *112*, 6156–6214.

(39) Pumera, M. *Chem. Soc. Rev.* **2010**, *39*, 4146–4157.

(40) Zheng, G.; Patolsky, F.; Cui, Y.; Wang, W. Y.; Lieber, C. M. *Nat. Biotechnol.* **2005**, *23*, 1294–1301.

(41) Laidler, K. J. *Chemical Kinetics*, 3rd ed.; Harper & Row: New York, 1987.

(42) Reuel, N. F.; et al. *ACS Nano* **2013**, *7*, 7472–7482.

(43) Margoliash, E. *Proc. Natl. Acad. Sci. U.S.A.* **1963**, *50*, 672–679.

(44) Chan, K. T.; Neaton, J. B.; Cohen, M. L. *Phys. Rev. B* **2008**, *77*, 235430.
(45) Chakarova-Kack, S. D.; Schroder, E.; Lundqvist, B. I.; Langreth, D. C. *Phys. Rev. Lett.* **2006**, *96*, 146107.
(46) Sato, F.; Yoshihiro, T.; Era, M.; Kashiwagi, H. *Chem. Phys. Lett.* **2001**, *341*, 645−651.
(47) Tkatchenko, A.; Von Lilienfeld, O. A. *Phys. Rev. B* **2006**, *73*, 153406.
(48) Umadevi, D.; Sastry, G. N. *J. Phys. Chem. C* **2001**, *115*, 9656−9667.
(49) Harlow, E.; Lane, D. *Antibodies: A Laboratory Manual*, 1st ed.; Cold Spring Harbor Laboratory Press: Plainview, NY, 1988.
(50) Voros, J. *Biophys. J.* **2004**, *87*, 553−561.
(51) Alwarappan, S.; Joshi, R. K.; Ram, M. K.; Kumar, A. *Appl. Phys. Lett.* **2010**, *96*, 263702.


dx.doi.org/10.1021/nl502279c | *Nano Lett.* XXXX, XXX, XXX−XXX